Simple synthesis of CoO–NiO–C anode materials for lithium-ion batteries and investigation on its electrochemical performance

Y.F. Wang, L.J. Zhang*

Departments of College of Environmental and Energy Engineering, Beijing University of Technology, Pingleyuan 100, Chaoyang District, 100124 Beijing, PR China

ABSTRACT

CoO–NiO–C nanocomposite materials with different morphology are successfully synthesized by using co-precipitation and subsequent pyrolytic carbon reduction method. The structure and morphology of obtained materials are investigated by X-ray diffraction (XRD), scanning electron microscopy (SEM), and transmission electron microscopy (TEM). The XRD patterns of samples display the diffraction peaks of $3CoO \cdot 5NiO$ cubic crystal. Moreover, the synthesis conditions which strongly impact on the morphology and electrochemical properties of the CoO–NiO–C materials are systematically investigated. When CoO–NiO–C materials are used as anodes for lithium ion batteries, the sample obtained at 600 °C exhibits the best cycling performance, which shows a reversible capacity about 562 mAh g^{-1} at the current density 100 mA g^{-1} after 60 cycles. On the other hand, this material also exhibits a superior rate performance. The excellent performance of samples could be attributed to the small and uniform particle size and introducing of metal oxides composite structure, which could improve the kinetic behavior and accommodate the volume changes during cycling.

© 2012 Elsevier B.V. All rights reserved.

1. Introduction

With the development of portable electronic products and vehicles, their support power sources with advantages of high-capacity, high-power, and recyclabllity are urgently needed. Compared with other secondary batteries, lithium ion battery has attracted much attention in recent years. Since Poizot et al. reported that transition metal oxides (TMOs) could be used as anodes for lithium ion battery [1], these materials have been widely concerned. However, the application of TMOs in practical batteries is hindered due to the capacity fading caused by large volume expansion during the cycling process and the low rate performance arising from kinetic limitations [2]. Thus, it was important to overcome these obstacles and develop novel strategies to improve the cycling capability and rate performance of TMOs.

Recently, it was reported that the hybrid metal oxides, such as SnO_2–CuO and ZnO–NiO, exhibited higher specific capacity and improved fading characteristics relatively to the single metal oxide [3–7]. This form of hybrid metal oxides could be simply expressed as MO–TMO, where MO represented all these metal oxides that could be used as anodes for lithium ion batteries, and TMO was used as a supporting and conducting matrix to buffer the volume change of the MO [7]. Li et al. [4] reported a novel CuO-nanotubes/SnO_2

composite which showed higher reversible capacity, better durability, and high rate performance than the pure SnO_2. It was found that the CuO-nanotubes were reduced to metallic Cu in the first discharge process, which could still retain tube structure of the CuO-nanotubes as a buffer to alleviate the volume expansion and also be a good tube conductor to improve the electrical conductivity of the electrode. As reported in the literature [3,8–10], metallic nanoparticles generated by TMOs in the discharge process could catalyze the decomposition of SEI in the charge process. In the MO–TMO material, there was often one transition metal oxide that could generate metallic nanoparticles. Therefore, the hybrid metal oxides that contained two transition metal oxides (expressed as TMO–TMO), with higher synergistic electrocatalytic behavior and the original advantages of MO–TMO, would exhibit even better electrochemical performance than the single metal oxide. Zhang et al. [6] reported a three-dimensional Li_2O–NiO–CoO composite thin-film electrode, that could exhibit a high reversible capacity (>800 mAh g^{-1}) at a cycling rate of 0.5 C and good capacity retention as well as outstanding rate capability. However, there were only a few reports on the application of TMO–TMO as anode materials for lithium-ion batteries [5,6].

In this paper, we report a novel and large scaled CoO–NiO–C composite materials prepared by co-precipitation and subsequent pyrolytic carbon reduction methods [11]. Glucose was added as carbon source to reduce Co^{3+} to Co^{2+} and Ni^{3+} to Ni^{2+} [12], and the excess carbon could also be embedded in particles to increase conductivity and hinder the growth of nanoparticles [13].

Table 1
Experimental parameter of the control experiments.

Number	NiCl$_2$·6H$_2$O (mmol)	CoCl$_2$·6H$_2$O (mmol)	Glucose (g)	Calcined temperature (°C)	Calcined atmosphere	Calcined time (h)
Sample-1	20	20	–	600	Ar	4
Sample-2	40	–	–	600	Ar	4
Sample-3	–	20	–	600	Ar	4
Sample-4	20	20	1.2	600	Ar	6

Some interesting findings, which were different from common single metal oxides, were discovered during this study. When the CoO–NiO–C materials were used as anodes for lithium ion batteries, the sample obtained at 600 °C exhibited the best cycling performance. Compared with the reported NiO and CoO, the CoO–NiO–C composite material showed enhanced lithium storage capacity. The excellent performance of sample could be attributed to the small and uniform particle size and the existence of metal oxide composite structure, which could improve the kinetic behavior and accommodate volume changes during cycling. We believed that the synthesized CoO–NiO–C composites would be a potential anode material to pair the high voltage cathode material for high energy-density lithium-ion batteries in the future.

2. Experiment

All the chemical reagents were analytically pure and used without further purification. The reaction mechanism had been reported somewhere [14]. In a typical synthesis, 20 mmol nickel chloride and 20 mmol cobalt chloride were firstly dissolved into 60 mL distilled water under continuous stirring at 50 °C in water bath, then, 10 mL ammonia (25 wt.%) was dropped into the above solution. After 1 h, 30 mL 0.25 M potassium persulfate solution was added and kept in 50 °C water bath with stirring for 6 h. The precursor was filtered and dried in vacuum at 80 °C for 12 h. Subsequently, 1.2 g precursor powder was immersed into 100 mL glucose aqueous solution (12 g L^{-1}) with stirring for 6 h, then, the intermediate product was filtered and dried in vacuum at 80 °C for 12 h. Finally, the intermediate product was calcined at different temperatures from 500 °C to 700 °C for 4 h in an electrical furnace in Ar. Products obtained at 500 °C, 600 °C and 700 °C were defined as S-500, S-600, and S-700, respectively.

To examine the influence of synthesis conditions on the morphology, structure, and electrochemical properties of obtained materials, four control experiments were designed, and the experiment parameter was shown in Table 1. Products obtained from control experiments were defined as Sample-1, -2, -3 and -4 (Table 1).

The obtained products were characterized by X-ray diffraction (XRD, BRUKER D8 ADVANCE, Cu K$_\alpha$ radiation), scanning electron microscopy (SEM, Hitachi S-3400 NSEM), SEM–EDS analysis, and transmission electron microscopy (TEM, JEOL JEM-2010). Thermo gravimetric analysis (TGA) was carried out on a Seiko Instruments 6300 TG-DTA device with a heating rate of 10 °C min^{-1} in Ar.

The working electrodes were composed of 80 wt.% of active material, 10 wt.% of acetylene black, and 10 wt.% of the binder (poly(vinylidene difluoride), PVDF). These materials were dissolved in N-methyl pyrrolidone and formed homogeneous slurry, then, slurry was spread onto the nickel foam. After vacuum drying at 80 °C for 12 h, the foam was pressed under a pressure of 20 MPa. The weight of active materials was about 2 mg cm^{-2}. Coin cells (CR2032) were assembled in an argon filled glove box. Li foil was used as counter electrode, and polypropylene film (Celgard 2300) was used as separator. The electrolyte was 1 M LiPF$_6$ in a mixture of ethylene carbonate (EC) and diethyl carbonate (DEC) (1:1 by volume). Coin cells were cycled galvanostatically in the voltage range between 0.002 and 3 V at a current density of 100 mA g^{-1} with

a multichannel battery test system (NEWARE). Cyclic voltammetry measurements were conducted with a VMP3 Electrochemical Workstation at the scanning rate 0.5 mV s^{-1} between 0 and 3 V (versus Li/Li$^+$). The electrochemical impedance spectroscopy (EIS) of the electrode was also measured on the VMP3 Electrochemical Workstation. Before the EIS measurement, the electrode was cycled for five times and kept until the open-circuit voltage reached stable. The excitation voltage applied to the cells was 5 mV and the frequency ranged from 100 MHz to 100 kHz. For comparison, the EIS data was normalized referred per unit of mass.

3. Results and discussion

Fig. 1 shows the XRD patterns of samples prepared at different temperature. All peaks were corresponding to the 3CoO·5NiO (JCPDS Card No.00-003-0984) phase. Different from the multiphase patterns of hybrid metal oxides materials reported in the literature [3–5,7], it was single phase here. No peaks ascribed to C were detected by XRD; however, the result of SEM–EDS analysis confirmed the existence of carbon.

Fig. 2 demonstrates the SEM–EDS images, which overlapped the SEM images with the corresponding EDS mappings of element C. The red spots represented the presence of C element in SEM–EDS images. It obviously indicated that the distribution of carbon in these three products was homogeneous. The amount of red spot for S-600 (shown in Fig. 2B) was less than those in another two samples (in Fig. 2A and C), which indicated the carbon content in S-600 was lowest. EDS results showed the carbon content was 5.4%, 2.22%, and 6.9% for S-500, S-600, and S-700, respectively.

Fig. 3 shows the TG curves of the final products from 20 °C to 1000 °C with a heating rate of 10 °C min^{-1} in Ar. TG analysis was used to determine the chemical composition of the final products [15]. In the initial weight loss between 30 and 150 °C was mainly caused by the removal of adsorbed water, while the weight loss (150–600 °C) in the second region could be attributed to the decomposition of C—H bonds and oxygen-containing groups [16].
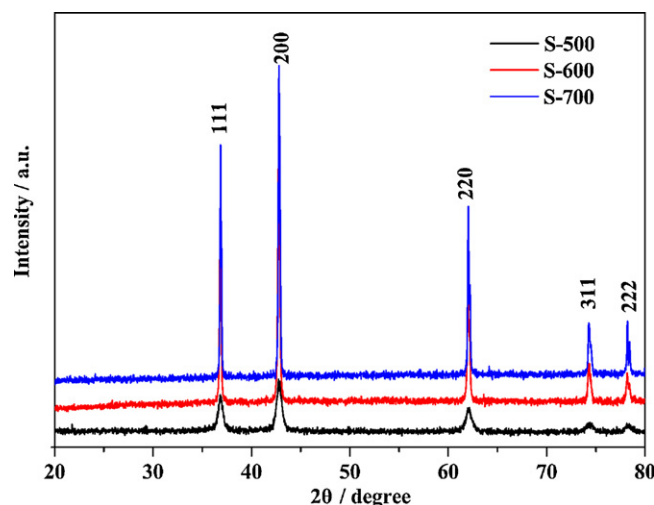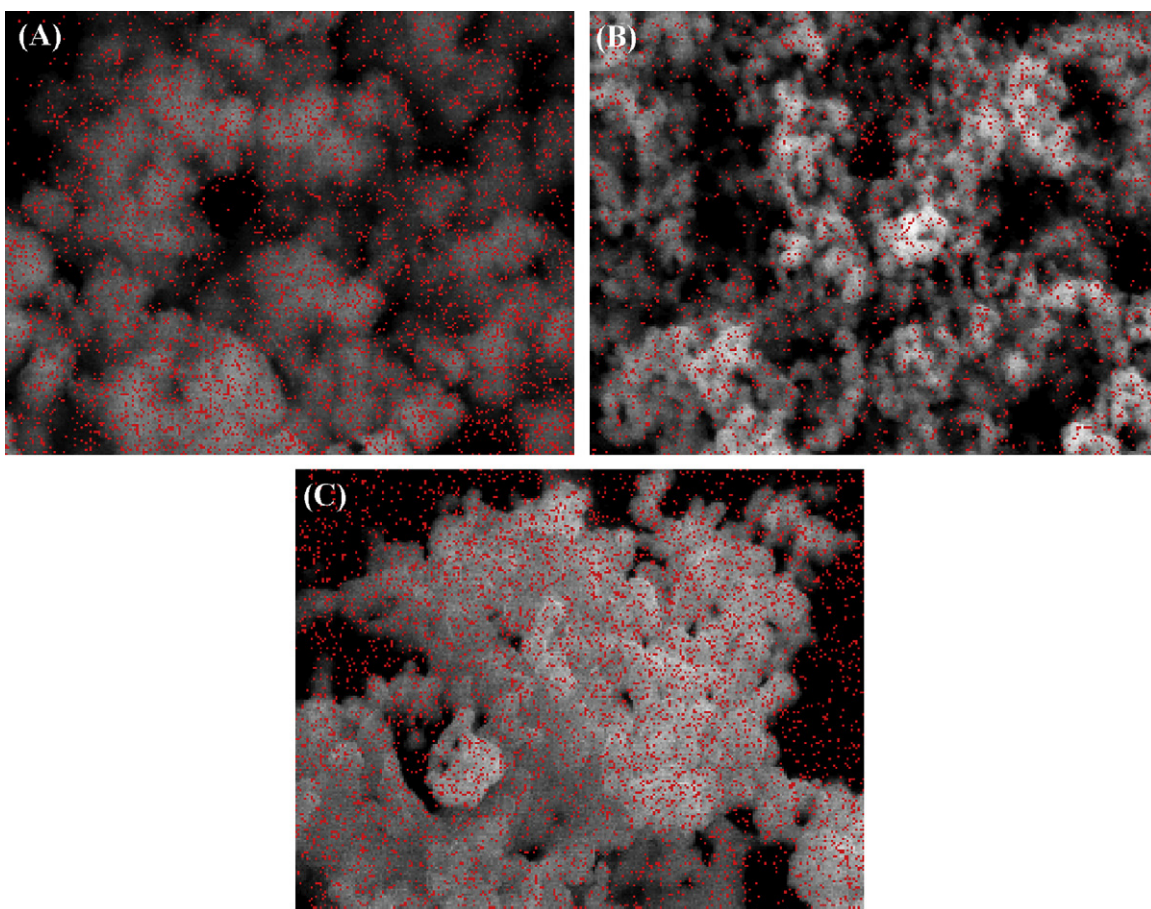

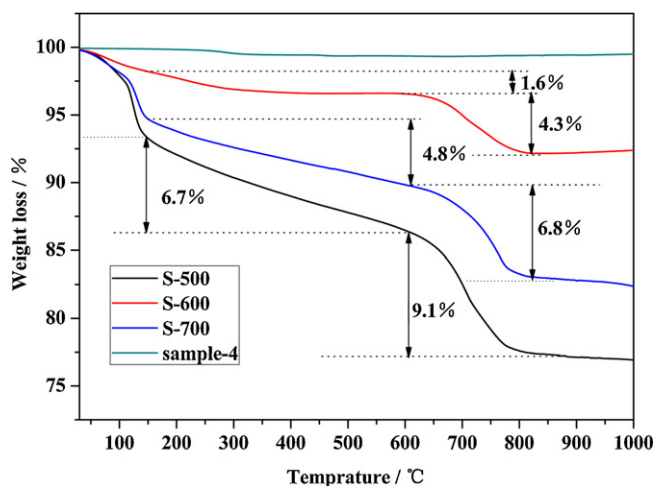**Fig. 1.** XRD patterns of samples obtained at different temperature.

Fig. 2. SEM–EDS images of samples obtained at different temperature (A) S-500, (B) S-600, and (C) S-700. The red spots represented the presence of C element in SEM–EDS images. (For interpretation of the references to color in this figure legend, the reader is referred to the web version of the article.)

The weight loss in the third region between 600 and 850 °C could be attributed to the carbonizing process [16]. So the weight loss between 150 and 850 °C was related to the carbon content in the final product. Interestingly, the overall weight loss in this region for S-600 was only 5.9% much smaller than that S-500 (15.8%) and S-700 (11.6%). It might indicate S-600 had the lowest carbon content. And the EDS results confirmed this surmise. We proposed that this result was caused by the different chemical reactivity and the

reactivity at 600 °C was the highest. Compared with 500 °C and 700 °C, when the precursor was calcinated at 600 °C, more glucose would be spent to support the reduction reaction and hinder the nanoparticles from growing up. After calcation, the residual carbon (that contained C—H bonds and oxygen-containing groups [16]) content would be lowest for S-600. When tested by TG analysis, the overall weigh loss corresponding to the decomposition of C—H bonds and oxygen-containing groups for S-600 would be smallest among these three samples. This surmise was consistent with the results of TG, EDS, and SEM–EDS images. TG curve for Sample-4 (calcined at 600 °C for 6 h) was almost flat which represented the decomposition of carbon source was precious little. EDS result showed the carbon content of Sample-4 was only 1.84%, which further confirmed the reactivity at 600 °C was highest.

Fig. 4 shows the SEM images of samples obtained at different temperature. It could be seen that various shapes of products were obtained by changing the calcination temperature. Fig. 4A showed the precursor was 3D flower-like sphere architecture approximately 500 nm in diameter, and several dozens of petal-like nanoflakes aggregated into the sphere. In Fig. 4B, S-500 showed the similar morphology with the precursor. With the calcination temperature increasing, the morphology of products became more and more diverse. S-600 exhibited graininess morphology with the particle size around 200 nm in diameter (Fig. 4C). When the calcination temperature reached 700 °C, the as prepared product was composed of sphere and polyhedron particles (Fig. 4D) and the particle size was not uniform. As reported in the literature [17,18], the changes of morphology related to the crystal strength of material. According to the XRD results, S-600 and S-700 were better

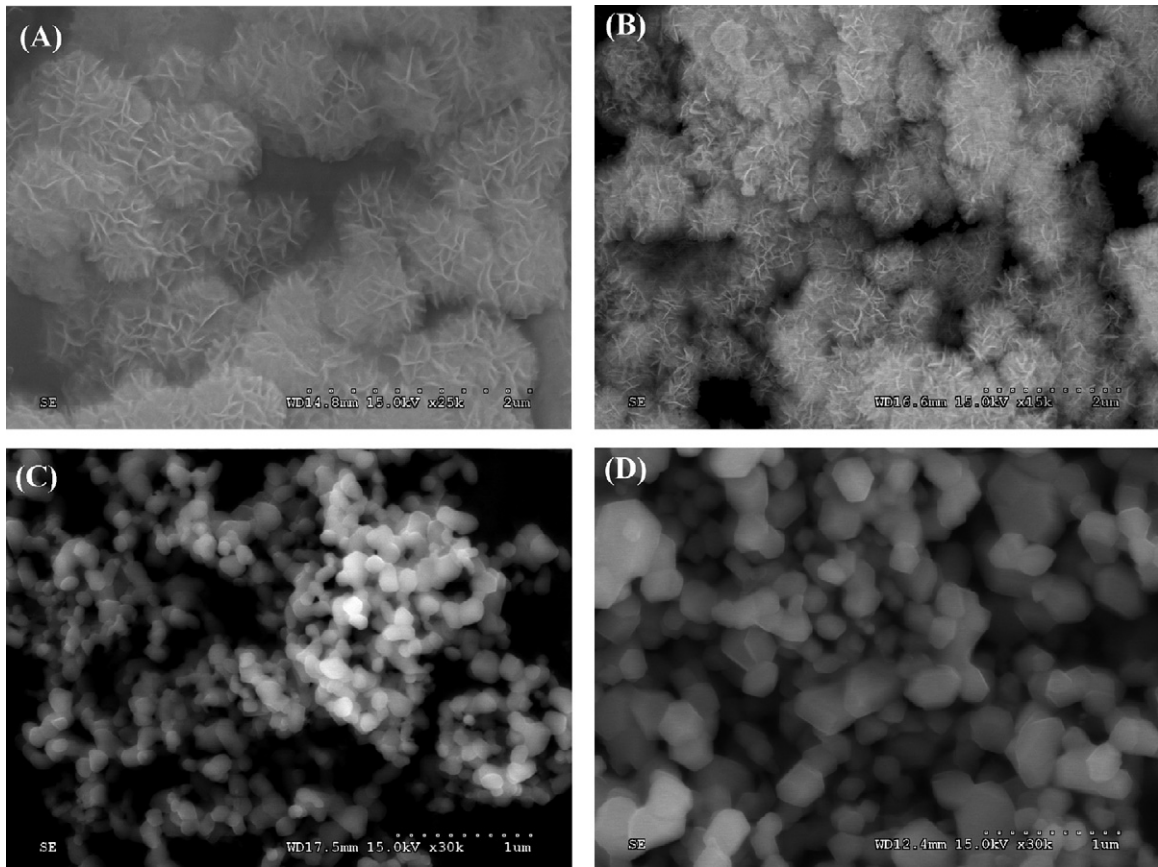**Fig. 3.** TG curves of the final product from 20 °C to 1000 °C with a heating rate of 10 °C min⁻¹ in Ar.

Fig. 4. SEM images of samples obtained at different temperature (A) precursor, (B) S-500, (C) S-600, and (D) S-700.
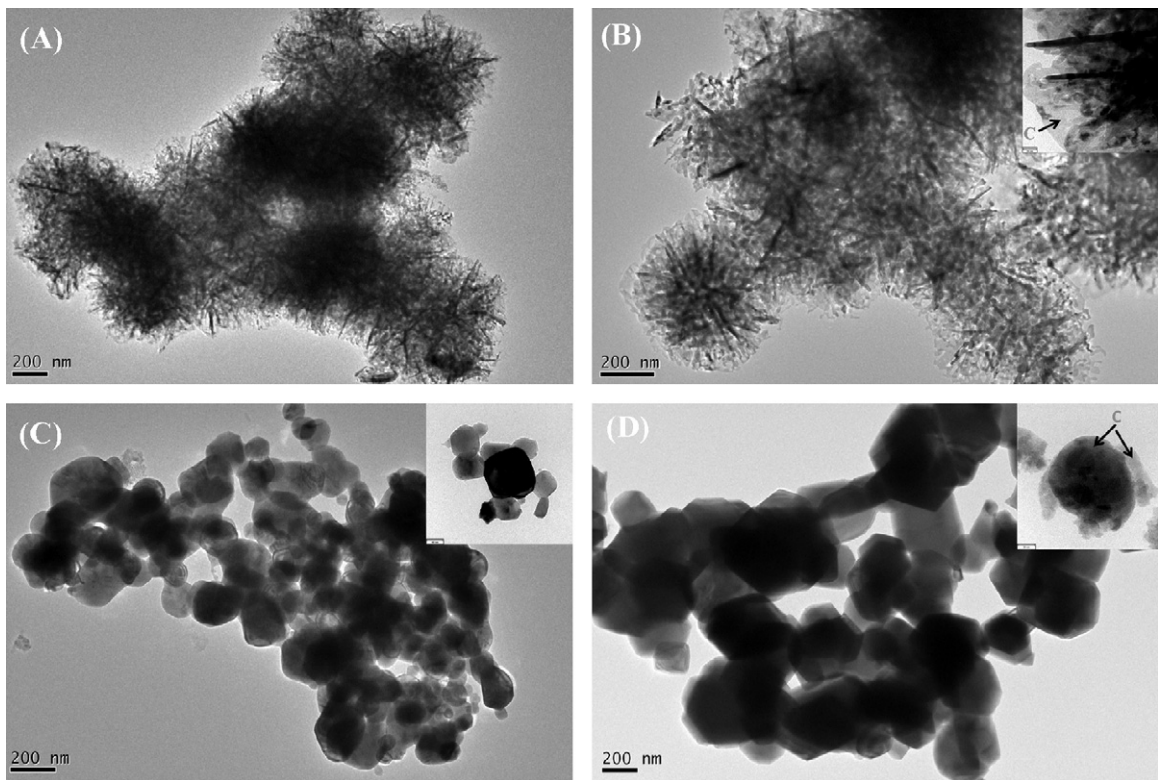

Fig. 5. TEM images of samples obtained at different temperature (A) precursor, (B) S-500, the inset is the partial magnifying image of S-500, (C) S-600, the inset is the magnifying image of S-600, and (D) S-700, the inset is the magnifying image of S-700.
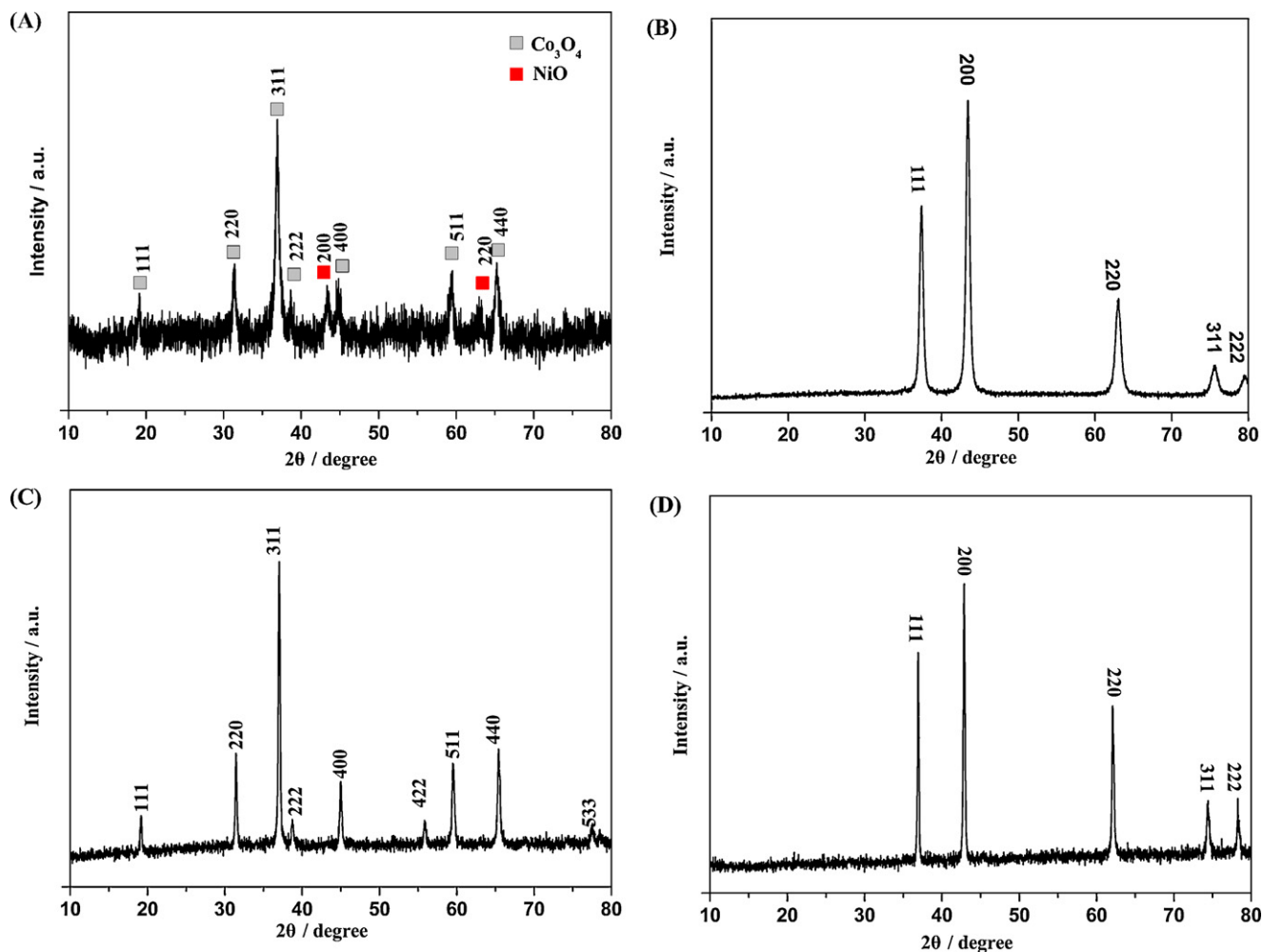
Fig. 6. XRD patterns of samples obtained in the control experiments (A) Sample-1, (B) Sample-2, (C) Sample-3, and (D) Sample-4.

crystallized with stronger peaks than S-500, hence, the precursor would suffer from stronger destroyed than 500 °C during the intense crystallization process (calcined at 600 °C or 700 °C), and the 3D flower-like sphere collapsed. Since glucose could serve not only as a reducing agent, but also a barrier to inhibit the growth of particles [19,20], with the higher reactivity, more regular and smaller particles were formed at 600 °C (Fig. 4C).

The transmission electron microscopy (TEM)characterization of samples prepared at different temperature are displayed in Fig. 5. It clearly demonstrated that the morphology of S-500 (Fig. 5B) was similar with the precursor (Fig. 5A). From the inserts in Fig. 5B and D, amorphous carbon could be found as shown by the arrows. However, it was not obvious in S-600 (Fig. 5C), which could be attributed to the low carbon content.

In order to investigate the effect of synthesis conditions on the morphology, structure and electrochemical properties, four control experiments were designed. To explore the influence of glucose, Sample-1was designed, while Sample-2 and Sample -3 were used to study the effects of nickel and cobalt salt, and Sample-4 was selected to investigate the influence of calcination time.

Fig. 6 shows the XRD patterns of samples obtained from the control experiments. In Fig. 6A, Sample-1 was multiphase pattern, the peaks were corresponding to cubic Co_3O_4 (JCPDS Card No. 42-1467) and cubic NiO (JCPDS Card No. 47-1049). The result indicated that the crystal structure of 3CoO·5NiO would not be obtained without glucose. In the XRD pattern of Sample-2 (Fig. 6B) only the peaks of NiO were observed. In Fig. 6C, all the peaks for Sample-3 were corresponding to the cubic Co_3O_4 (JCPDS Card No. 42-1467). 3CoO·5NiO crystal structure was obtained for Sample-4 as shown in Fig. 6D.

Fig. 7 is the SEM images of samples obtained from the control experiments. In Fig. 7A, Sample-1 exhibited 3D flower-like morphology as the precursor (Fig. 3A); however, some factions of collapsed spheres were observed. Sample-2 was faviform structure with serious aggregation as shown in Fig. 7B. In Fig. 7C, it could be clear seen that Sample-3 was composed of small particles and nano-rods. The particles were about 50 nm in diameter and the nano-rods were approximately 300 nm in length. Compared with S-600, Sample-4 had larger particle size (200 nm) as shown in Fig. 7D. Based on the above investigation, the following conclusions could be drawn. Firstly, glucose was essential to form the 3CoO•5NiO crystal structure. Secondly, when nickel salt was used only, the obtained sample was prone to form faviform structure. Thirdly, when cobalt salt was used only, the final product tended to form granular morphology. Lastly, the particle size would be increased with the increasing of calcination time.

Fig. 8 shows the discharge/charge curves for CoO–NiO–C electrodes at a current density of 100 mA g^{-1}. The first discharge specific capacity for S-500, S-600 and S-700 between 0.002 and 3 V was 976 mAh g^{-1}, 1125 mAh g^{-1} and 1127 mAh g^{-1}, respectively. And the corresponding initial columbic efficiency was 70.38%, 64.81%, and 59.41%. The extra capacity compared with the theoretic capacity of NiO (718 mAh g^{-1}) and CoO (716 mAh g^{-1}) resulted from the formation of SEI in the first discharge process [21]. And the
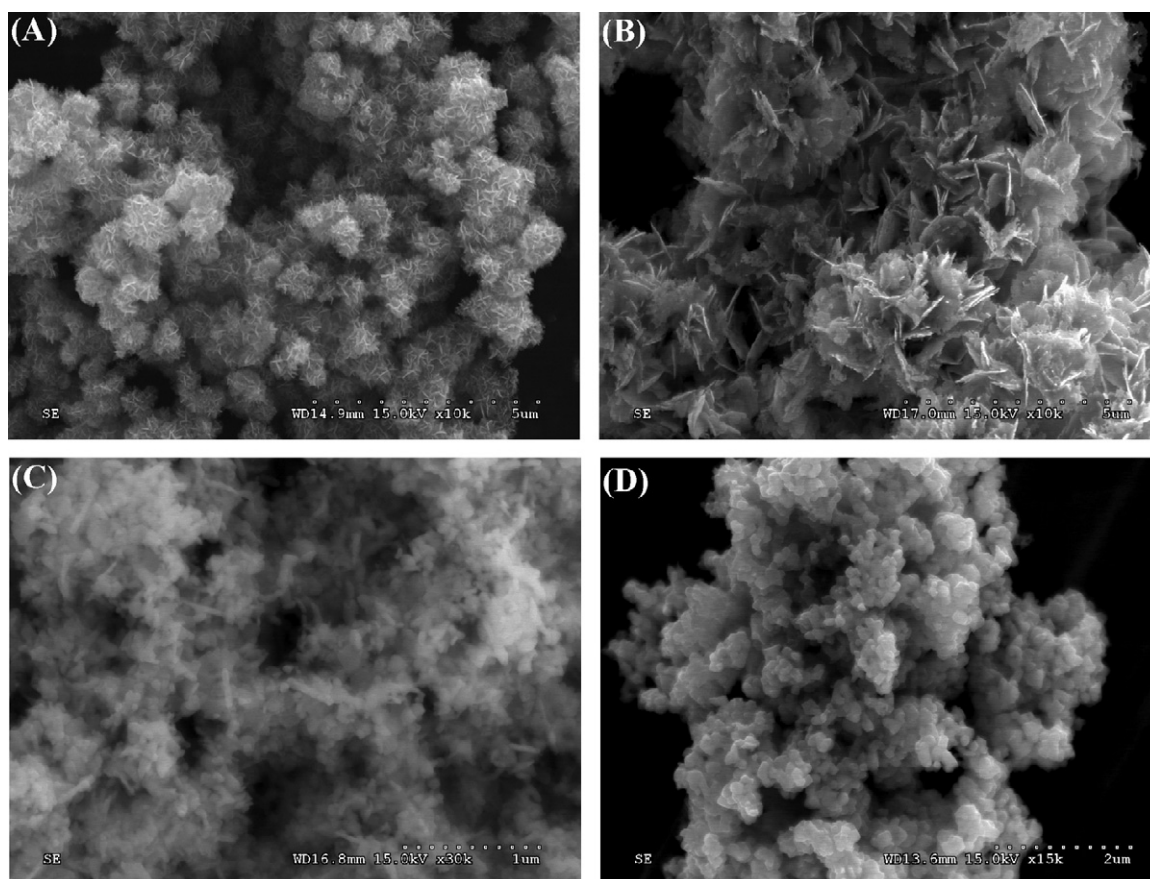
Fig. 7. SEM images of samples obtained in the control experiments (A) Sample-1, (B) Sample-2, (C) Sample-3, and (D) Sample-4.

incomplete decomposition of SEI was always the main reason for the low initial columbic efficiency found in transition metal oxides [19]. Due to the existence of amorphous carbon could reduce the specific surface area, less SEI would form for the product with higher carbon content during the discharge process [22]. The large particle size and high carbon content made the specific surface area of S-500 decrease, and resulted in the less formation of SEI. It could be used to explain that S-500 with the highest carbon content exhibited the highest initial columbic efficiency. As reported in the literature [3,8–10], Ni and Co nanoparticles generated during the discharge process could catalyze the decomposition of SEI in the charge process. On the other hand, samples with smaller particle sizes could generate smaller Ni and Co nanoparticles [23], which often possessed higher catalytic property than larger ones. Therefore, more SEI would decompose when it was catalyzed by the smaller nanoparticles and the irreversible capability could be obviously reduced. Although the carbon content was much lower, S-600 with the smaller particle size still showed higher initial columbic efficiency than S-700. For all these three samples, the first discharge curves showed an abrupt drop in potential down to about 0.71 V, followed with a long plateau between 0.71 V and 0.59 V corresponding to the decomposition of oxides into Ni and Co and the formation of amorphous Li_2O and SEI. However, the first discharge–charge curves for S-500 was difference from the others two samples. In Fig. 8A, there was a visible slop at 1.11 V–0.71 V, which was not detected in the other two samples. And two inclined plateaus near 1.74 V and 2.34 V corresponding to the decomposition of SEI and the reoxidation of Ni and Co could be observed in the first charge curve. However, only the inclined plateaus near 2.2 V could be found in Fig. 8B and C. The detail needed to be further examined. Fig. 8D is the discharge/charge curves for S-600 between

0.002 and 2 V at a current density of $100\,mA\,g^{-1}$. From the initial charge curve it could be clearly seen that the first charge capacity was much lower than that in the voltage range between 0.002 and 3 V. It is well know that the capacity of this kind of materials is determined by the amount of Li ions transformed between the anode and cathode. Since the decomposition of SEI and oxidation reaction mainly occurred at 2.2 V for our samples, the narrower voltage window caused the amount of Li ions generated during the charge process lower and thus reduced the first charge specific capacity. On the other hand, it indicated the amount of Li ions that were used to support the reduction reaction in the subsequent discharge process was reduced, which resulted in the decreasing of discharge capacity. As shown in Fig. 8D, the second discharge capacity was $388\,mAh\,g^{-1}$ much lower than that cycled between 0.002 and 3 V ($732\,mAh\,g^{-1}$). The decreasing of discharge capacity made the amount of Li_2O that could generate Li ions in the charge process lower than that in the wider voltage window. As the increasing of cycling times, the amount of Li ions transformed between the anode and cathode was less and less. Therefore, the discharge/charge capacities were decreased more significantly during the cycles and the reversible capacity retention was much lower than that in the wider voltage window. As shown in Fig. 8A–D, after 60 cycles the reversible capacity retention for S-500, S-600, S-700 and S-600 cycling between 0.002 and 2 V was 27.4%, 76.8%, 73.2% and 35.3%, respectively. The reversible capacity retention was related to the cycling performance of these samples. It demonstrated S-600 with the highest reversible capacity retention might have the best cycling performance.

The cyclic voltammogram curves of CoO–NiO–C electrodes at a scan rate of $0.5\,mV\,s^{-1}$ are shown in Fig. 9. The cathodic and anodic peaks were all corresponding well to the discharge/charge
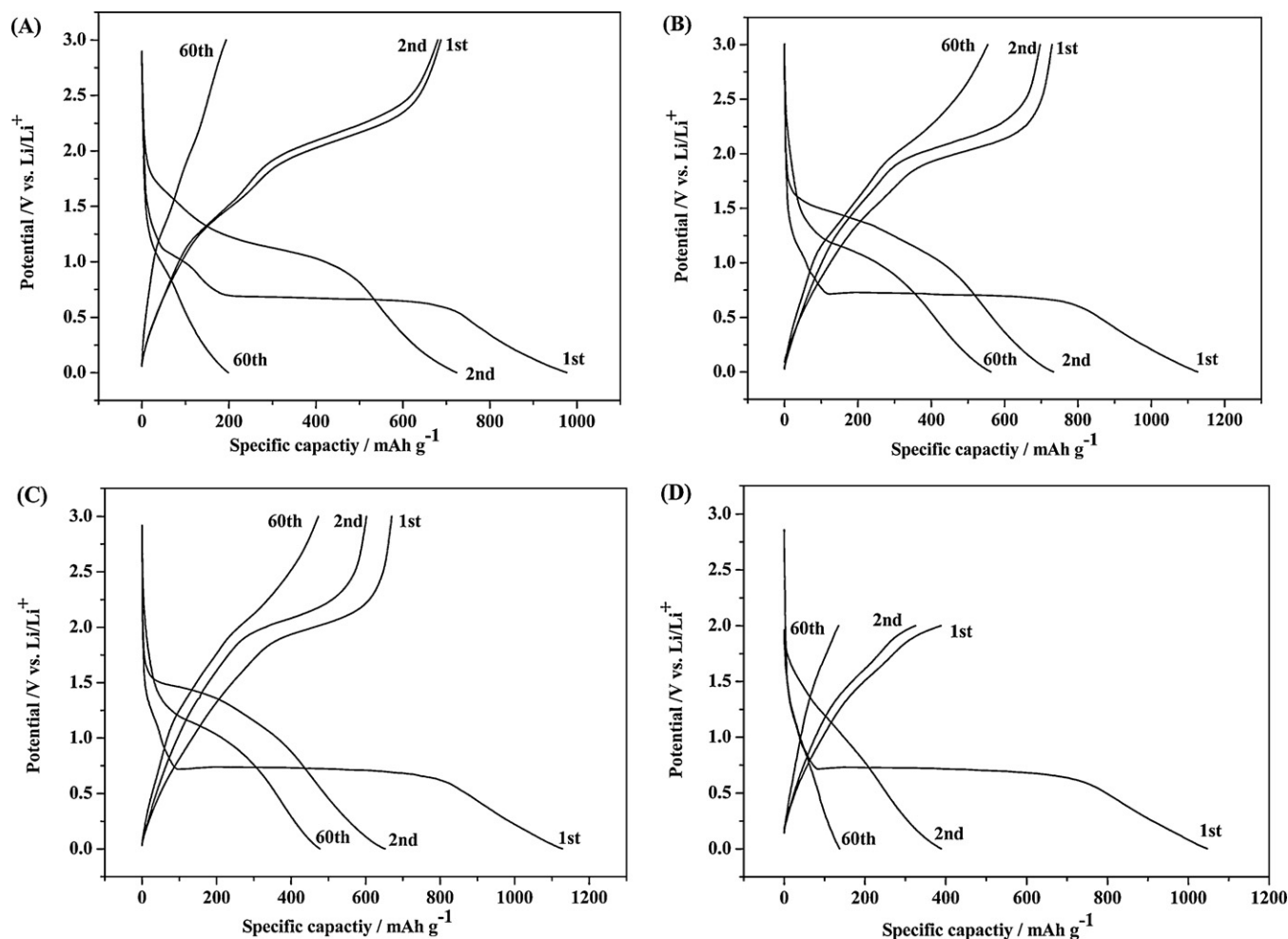
Fig. 8. Discharge–charge curves of samples obtained at different temperature (A) S-500, (B) S-600, (C) S-700, (D) S-600 cycling between 0.002 and 2 V.

plateaus as shown in Fig. 8. Interestingly, the shape of CV curves for S-500 (Fig. 9A) was semblable to that of NiO [8], while S-600 and S-700 (Fig. 9B and C) were similar to CoO [24]. The interval between the cathodic and anodic peaks could be used to suggest the polarization of the electrode material [3]. In the second scan of the CV curves, the separation between the cathodic and anodic peaks (ΔU) [22] for S-500, S-600 and S-700 was 1.49 V, 0.99 V and 1.01 V, respectively. Therefore, the polarization of S-600 was the weakest among these three samples. This result could also be further verified by the impedance spectra shown in Fig. 10. It could be predicted that samples with the weak polarization would exhibit good cycle stability.

Fig. 10 shows the AC impedance spectrum of samples obtained at different temperature. Before the measurement, the electrodes were cycled for five times and kept until the open-circuit voltage reached stable. The excitation voltage applied to the cells was 5 mV and the frequency ranged from 100 MHz to 100 kHz. For comparison, the EIS data was normalized referred per unit of mass. All profiles exhibited a semicircle in the mid-frequency region and a straight line in the low frequency region. The mid-frequency region was attributed to the charge transfer process, and the value of semicircle diameter gave an approximate indication of the charge transfer resistance [25]. The results of the AC impedance spectrum confirmed that S-600 with the smallest semicircle diameter had the lowest charge transfer resistance among these three samples. Compared with S-500 and S-700, the excellent electron conductivity of S-600 might be caused by the small particle size [26,27] and the Ni

and Co nanaoparticles generated in the first discharge process as reported in the hybrid MO–TMO materials [3–7]. This result was in accordance with the CV results.

The cycling performance of samples at the current density of 100 mA g^{-1} was shown in Fig. 11. Compared with S-500, both of S-600 and S-700 exhibited relatively better cycle stability, which was in accordance with the result of discharge/charge curves shown in Fig. 8. The poor cycle stability of S-500 could be attributed to the poor mechanical intensity of the flower-like architecture [28], which was easy to collapse caused by huge volume changes during cycles. Although the advantages of carbon modified hierarchically structured materials had been reported a lot in literature [19,20], the poor mechanical intensity of S-500 still made the electrochemical performance unsatisfied. After 60 cycles, S-500, S-600 and S-700 could deliver the reversible capacity of 198 mAh g^{-1}, 562 mAh g^{-1}, and 476 mAh g^{-1}, respectively. As the reported MO–TMO materials, high reversible capacity of both S-600 and S-700 could be attributed to the conductive and catalytic effects of Ni and Co nanoparticles formed in the first discharge process. Since the theoretic specific capacity of carbon (372 mAh g^{-1}) was much lower than NiO (718 mAh g^{-1}) and CoO (716 mAh g^{-1}), higher carbon content might make the specific capacity lower. Also, small and uniform particle size was beneficial to the cycling stability [26,29]. Therefore, S-600 with better conductivity, lower carbon content, smaller and more uniform particle size exhibited better cycle performance and higher reversible capacity than S-700. S-600 also showed enhanced lithium storage capacity compared with the
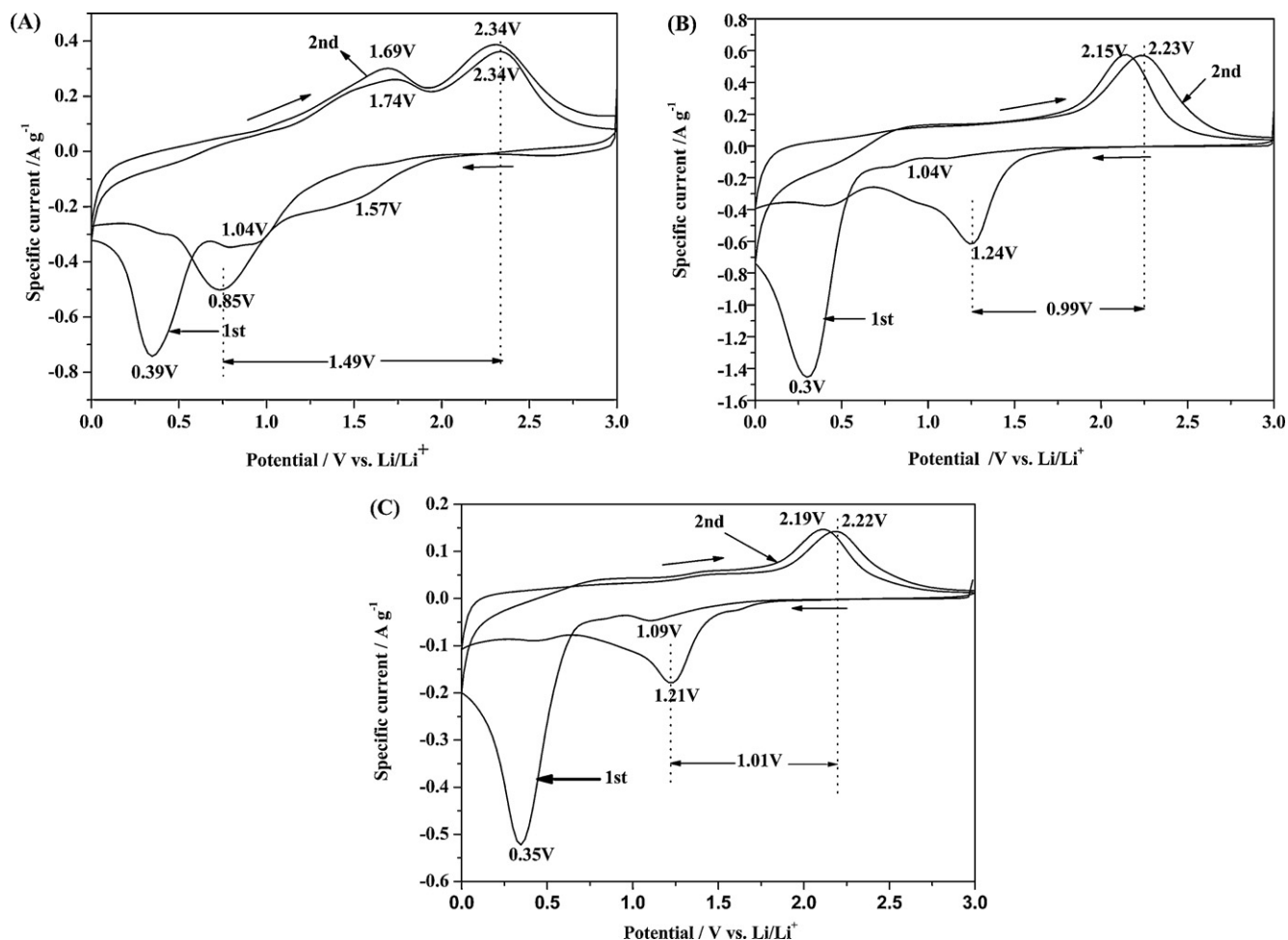
Fig. 9. Cyclic voltammograms of samples obtained at different temperature (A) S-500, (B) S-600, (C) S-700.

reported NiO and CoO composites [22,30,31,32]. The cycling stability of S-600 could even compare favorably with the Ti foil supported Co-doped NiO nanoflake arrays which possessed super electrode configuration [12]. Considering the application in practical batteries, the cycle performance of S-600 in the narrower voltage window 0.002–2 V was also measured as shown in Fig. 11. Compared with that cycled between 0.002 and 3 V, the cycle stability of the one cycled between 0.002 and 2 V was relatively worse, which was consistent with the result of the discharge/charge curves. After 60 cycles, it could deliver the reversible capacity 137 mAh g^{-1}. The lower reversible capacity and poorer cycling performance were due to the narrowed voltage window. As discussed before, the narrower voltage window could decrease the charge/discharge capacities and the reversible capacity retention significantly. It might indicate the voltage window of 0.002–3 V was more suitable for the application of this CoO–NiO–C material.

In the control experiments, the hybrid metal oxides materials were chosen to investigate the electrochemical performance. Fig. 12 shows the cycling performance of Sample-1 and -4. It demonstrated that the cycle stability of Sample-1 was much poorer than that of S-600 (shown in Fig. 9). After 60 cycles, the discharge capacity of Sample-1 was 58 mAh g^{-1}. The poor cycle stability was mostly due to the poor mechanical intensity of hierarchically structure. The crystal types might also affect the electrochemical performance. Sample-1 was multiphase pattern of Co$_3$O$_4$ with NiO, while S-600 was cubic structure 3CoO·5NiO. Compared with S-600, the discharge capacity of Sample-4 was much lower, which was 268 mAh g^{-1} after 60 cycles. The lower
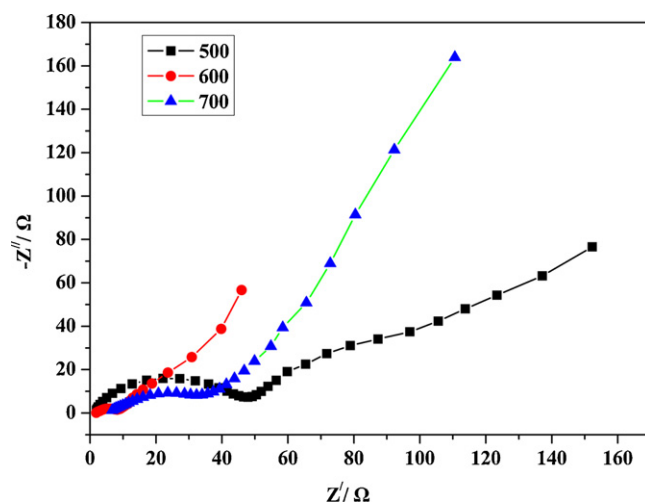

Fig. 10. AC impedance spectrum of samples obtained at different temperature.

reversible capacity could be attributed to the larger particle size [26].

Rate performance was important for the practicable application of the electrode material. S-600 with the best cycling performance in this study was chosen to test the rate performance. As shown in Fig. 13, after cycling at 0.28 C (200 mA g^{-1}), 0.7 C (500 mA g^{-1}), 1.4 C (1000 mA g^{-1}), 2.1 C (1500 mA g^{-1}) each for 10 times, S-600
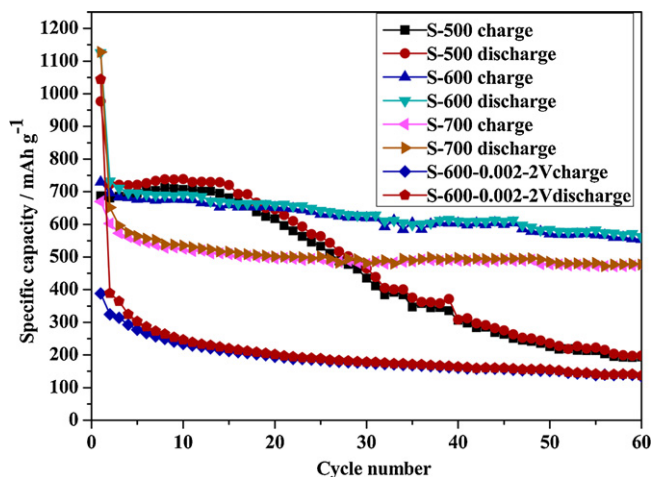
Fig. 11. Cycling performance of S-500, S-600 and S-700 at current density 100 mA g^{-1}. The curve of S-600-0.002–2 V represented the cycling performance of S-600 in the voltage window 0.002–2 V at current density 100 mA g^{-1}.
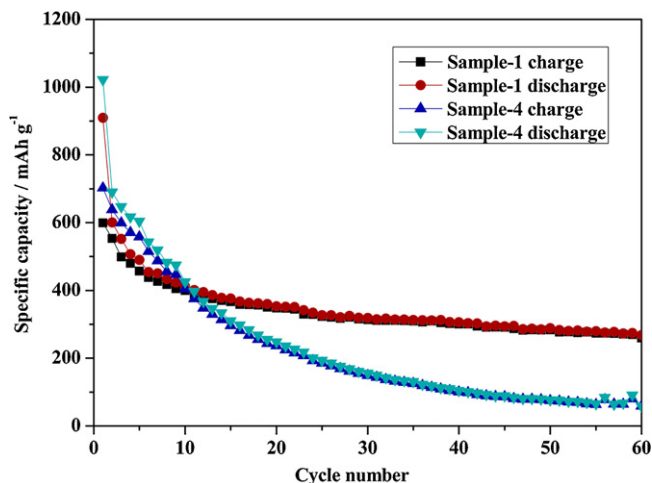

Fig. 12. Cycling performance of Sample-1 and Sample-4 at current density 100 mA g^{-1}.

could deliver the discharge capacities of 465 mAh g^{-1}, 291 mAh g^{-1}, 165 mAh g^{-1}, and 101 mAh g^{-1}, respectively. When the current density returned to 0.14 C (100 mA g^{-1}) and cycled for 10 times, the discharge capacity could still maintain 528 mAh g^{-1}. The reversible
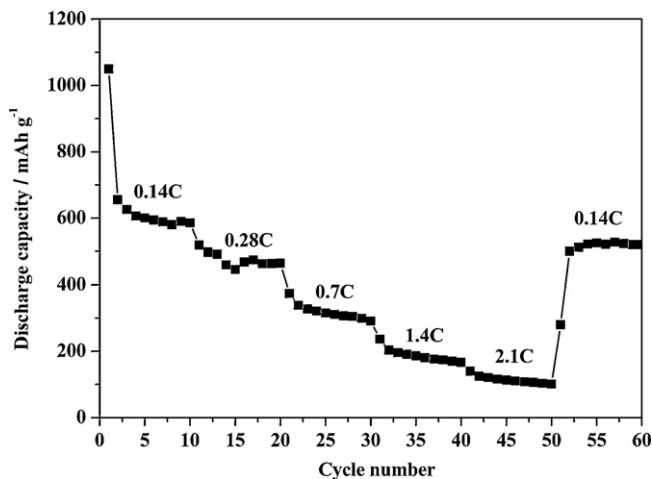

Fig. 13. Rate performance of S-600.

capacity retention was about 79.3%. Compared with the capacity retention of S-600 cycled at constant current density 100 mA g^{-1} (76.8%), the capacity retention after rate performance test was even a little higher, which represented the structure of the material did not been destroyed after high-current cycles. The excellent rate capability mainly depended on the small particle size and improved conductivity, which could short the diffusion path for ions and electrons, and be beneficial of the large current charge–discharge process.

4. Conclusion

CoO–NiO–C materials were successfully synthesized by co-precipitation and subsequent pyrolytic carbon reduction method. XRD results showed the synthetic material was cubic structure 3CoO·5NiO crystal. The different chemical reactivity resulted in carbon content and morphology variety in the final products. The results of control experiments showed the synthesis conditions had a great effort on morphology, structure, and electrochemical performance. The product obtained at 600 °C exhibited the best cycle stability and rate performance. The excellent performance of the sample could be attributed to the small and uniform particle size and introducing of metal oxides composite structure, which could improve the kinetic behavior and accommodate the volume changes during cycling. However, the low columbic efficiency of the sample still needed to be improved. Since the synthesis method was high yield as well as easy to be operated, we believed that the CoO–NiO–C material synthesized in this paper would be a promising anode material to pair the high voltage cathode for high energy-density lithium-ion batteries in the future.

References

[1] P. Poizot, S. Laruelle, S. Grugeon, L. Dupont, J.M. Tarascon, Nature 407 (2000) 496–499.
[2] S. Mitra, P. Poizot, A. Finke, J.M. Tarascon, Adv. Funct. Mater. 16 (2006) 2281–2287.
[3] Q.M. Pan, L.M. Qin, J. Liu, H.B. Wang, Electrochim. Acta 55 (2010) 5780–5785.
[4] C. Li, W. Wei, S.M. Fang, H.X. Wang, Y. Zhang, Y.H. Gui, R.F. Chen, J. Power Sources 195 (2010) 2939–2944.
[5] Y.N. NuLi, P. Zhan, Z.P. Guo, k.H. Liu, J. Yang, J.L. Wang, Mater. Res. Bull. 44 (2009) 140–145.
[6] P. Zhang, Z.P. Guo, S.G. Kang, Y.J. Choi, C.J. Kim, K.W. Kim, H.K. Liu, J. Power Sources 189 (2009) 566–570.
[7] M.F. Hassan, M.M. Rahman, Z.P. Guo, Z.X. Chen, H.K. Liu, J. Mater. Chem. 20 (2010) 9707–9712.
[8] X.H. Huang, J.P. Tu, B. Zhang, Y. Li, Y.F. Yuan, H.M. Wu, J. Power Sources 161 (2006) 541–544.
[9] X.H. Huang, Y.F. Yuan, Z. Wang, S.Y. Zhang, F. Zhou, J. Alloys Compd. 509 (2011) 3425–3429.
[10] J.Y. Xiang, J.P. Tu, Y.F. Yuan, X.L. Wang, X.H. Huang, Z.Y. Zeng, Electrochim. Acta 54 (2009) 1160–1165.
[11] J.P. Liu, Y.Y. Li, R.M. Ding, J. Jiang, Y.Y. Hu, X.X. Ji, Q.B. Chi, Z. Zhu, X.T. Huang, J. Phys. Chem. C 113 (2009) 5336–5339.
[12] Y.J. Mai, J.P. Tu, X.H. Xia, C.D. Gu, X.L. Wang, J. Power Sources 196 (2011) 6388–6393.
[13] Y.Z.Z.Z. Li, M.M. Ren, X.P. Gao, J. Yan, Mater. Lett. 61 (2007) 4562–4564.
[14] S.Y. Han, D.H. Lee, Y.J. Chang, S.O. Ryu, T.J. Lee, C.H. Chang, J. Electrochem. Soc. 153 (2006) C382–C386.
[15] F.F. Cao, X.L. Wu, S. Xin, Y.G. Guo, L.J. Wan, J. Phys. Chem. C 114 (2010) 10308–10313.
[16] X.K. Zhi, G.C. Liang, L. Wang, X.Q. Ou, L.M. Gao, X.F. Jie, J. Alloys Compd. 503 (2010) 370–374.
[17] Y. Liu, X.G. Zhang, Electrochim. Acta 54 (2009) 4180–4185.

[18] D. Larcher, G. Sudant, J.B. Leriche, Y. Chabre, J.M. Tarascon, J. Electrochem. Soc. 149 (2002) A234–A241.
[19] S.L. Jin, H.G. Deng, D.H. Long, X.J. Liu, L. Zhan, X.Y. Liang, W.M. Qiao, L.C. Ling, J. Power Sources 196 (2011) 3887–3893.
[20] F.D. Wu, Y. Wang, J. Mater. Chem. 21 (2011) 6636–6641.
[21] X.H. Huang, J.P. Tu, C.Q. Zhang, X.T. Chen, Y.F. Yuan, H.M. Wu, Electrochim. Acta 52 (2007) 4177–4181.
[22] X.H. Huang, J.P. Tu, C.Q. Zhang, J.Y. Xiang, Electrochem. Commun. 9 (2007) 1180–1184.
[23] X.J. Zhang, D.G. Zhang, X.M. Ni, J.M. Song, H.G. Zheng, J. Nanopart. Res. 10 (2008) 839–844.
[24] J. Jiang, J.P. Liu, R.M. Ding, X.X. Ji, Y.Y. Hu, X. Li, A.Z. Hu, F. Wu, Z.H. Zhu, X.T. Huang, J. Phys. Chem. C 114 (2010) 929–932.

[25] H. Liu, G.X. Wang, J. Park, J.Z. Wang, H.K. Liu, C. Zhang, Electrochim. Acta 54 (2009) 1733–1736.
[26] Y.Y. Liu, C.B. Cao, Electrochim. Acta 55 (2010) 4694–4699.
[27] Z.H. Xu, L. Xu, Q.Y. Lai, X.Y. Ji, Mater. Chem. Phys. 105 (2007) 80–85.
[28] L. Liu, Y. Li, S.M. Yuan, M. Ge, M.M. Ren, C.S. Sun, Z. Zhou, J. Phys. Chem. C 114 (2010) 251–255.
[29] J.S. Chen, X.W. Lou, J. Power Sources 195 (2010) 2905–2908.
[30] H. Qiao, L.F. Xiao, Z. Zheng, H.W. Liu, F.L. Jia, L.Z. Zhang, J. Power Sources 185 (2008) 486–491.
[31] H.W. Lu, D. Li, K. Sun, Y.S. Li, Z.W. Fu, Solid State Sci. 11 (2009) 982–987.
[32] X.H. Huang, J.P. Tu, C.Q. Zhang, F. Zhou, Electrochim. Acta 55 (2010) 8981–8985.